PHYSICAL REVIEW B VOLUME 47, NUMBER 12 15 MARCH 1993-II

Resonant photoemission in CeNi single crystals

T. Kashiwakura, S. Suzuki, T. Okane, and S. Sato
Department of Physics, Tohoku University, Sendai 980, Japan

T. Kinoshita, A. Kakizaki, and T. Ishii
Institute for Solid State Physics, University of Tokyo, Tokyo 106, Japan

Y. Isikawa
College of Liberal Arts, Toyama University, Toyama 930, Japan

H. Yamagami
College of General Education, Tohoku University, Sendai 980, Japan

A. Hasegawa
College of General Education, Niigata University, Niigata 950-21, Japan

(Received 15 July 1992)

The valence-band photoemission of the (010) surfaces of CeNi single crystals has been observed. The features occurring in angle-resolved normal-emission spectra do not show an appreciable amount of dispersion. The energy distribution curves are squeezed and narrower than those suggested by an existing energy-band calculation. Resonant photoemission has been observed both near the $3p$ core electron excitation threshold of Ni and the $4d$ threshold of Ce. An aspect of the super-Coster-Kronig final state with a post-collision interaction is found near the onset of the resonance in the two-hole bound-state satellite. In addition to the two-peak profile in the overall spectral aspect of the $4f$ spectrum, two additional features are resolved. The origin of these features is discussed. The ratio of Fano's q parameters between the $3p$-$3d$ resonance in Ni ions and the $4d$-$4f$ resonance in Ce ions agrees with a result of a simple theoretical analysis.

I. INTRODUCTION

Valence-band photoelectron spectroscopy using synchrotron radiation is one of the most powerful tools for investigating the electronic structures of valence-fluctuating rare-earth compounds, where $4f$ states of a rare-earth ion are occupied by a nonintegral number of electrons.[1-4] In the investigation of Ce and its compounds by means of valence-band photoelectron spectroscopy, we have been concerned mainly with the electronic structures of Ce $4f$ electrons to which anomalous thermal, electric, and magnetic properties, as well as the Kondo volume collapse, have been ascribed. The contribution of Ce $4f$ electrons to a valence-band photoelectron spectrum can be extracted by utilizing the existence of a maximum in the photon-energy dependence of the $4f$ partial photoionization cross section and the resonant photoemission, which occurs near the inner-shell electron excitation threshold of cerium.[4-18] The photoelectron spectra with the He resonance lines have been used to analyze the Ce $4f$ contribution to the photoelectron spectra with high resolution.[19,20] The specific aspect of the $4f$ spectra of Ce compounds is the two-peak profile. One peak occurs at the Fermi edge and the other between 2 and 3 eV below it. Although the energy-band theory often explains the overall profiles of the photoelectron energy distribution curves (EDC's), the occurrence of the two-peak profiles of the $4f$ spectra could not be explained by the energy-band theory without considering the excitation of the system.[21-23]

Many theoretical works for explaining the two-peak profile of $4f$ spectra have been reported.[21-35] Many of the theories are based on more or less similar physical pictures, and Ce $4f$ spectra are calculated using the impurity Anderson Hamiltonian. In the theories, the hybridization between Ce $4f$ states and the conduction-electron states plays a crucial role. In the case of insulators such as halides, the hybridization takes place between the Ce $4f$ states and the valence states of neighboring negative ions.[24,25] In principle, three kinds of electronic configurations, $4f^0L$, $4f^1\underline{L}$, and $4f^2\underline{L}^2$ are important in the ground state. Here, L represents the filled conduction band, $\underline{L}$ the state with a hole in the conduction band, and $\underline{L}^2$ the state with two holes. The existence of the three configurations, $4f^0L$, $4f^1\underline{L}$, and $4f^2\underline{L}^2$, in the ground state is strongly suggested by x-ray photoemission spectroscopy (XPS) core-level spectra. In the limit of large intra-atomic Coulomb energy, U, of $4f$ electrons, the $4f^2\underline{L}^2$ configuration does not actually occur, and the major qualitative aspects of $4f$ spectra in the valence-band region are expressed in this limiting case. Most calculations are made using only $4f^0L$ and $4f^1\underline{L}$ configurations in the ground state. Since the $4f$ state is N_f-fold degenerate, the basis state from the $4f^1\underline{L}$ configuration includes a linear combination of the product of the substates and component states of the hybridized conduction band. The summation is made over all $4f$ substates and the whole hybridized conduction-band states. The coefficients of the linear combination, which make an important contribution to the $4f$ spectrum, are obtained by numerically solving integral equations derived from the impurity Anderson Hamiltonian. The fluctuating valence is expressed by the configuration mixing, where one configuration corresponds to one basis function.

In most cases, the $4f$ spectra are calculated using one-particle Green's functions in the resolvent formalism. Major emphasis has been placed on clarifying the mechanism of the formation of the Kondo peak at the Fermi edge. A typical example is found in the article by Gunnarsson and Schönhammer.[26,27] They used the $1/N_f$ expansion idea in the limit of large N_f.[36] The emission of a $4f$ electron causes the transition $4f^1\underline{L} \rightarrow 4f^0\underline{L}$. Since the $4f^0\underline{L}$ state mixes with the $4f^1\underline{L}^2$ state through the hybridization, substates arising from these two kinds of configurations exist in the final state and the matrix elements between them crucially affect the energy dependence of the Green's function. The energy difference between the interacting and the noninteracting ground states almost cancels out the renormalized $4f$ energy, and the $4f$ spectral weight has a pole at an energy that is almost vanishing. This gives rise to the sharp Kondo peak. The appearance of the second peak is not so obvious as that of the Kondo peak. Mathematically, the second peak is introduced by the renormalized $4f$ level, which causes another minimum in the denominator of the spectral function, and the hybridization modifies it so that the oscillator strength is transferred to the Kondo peak region. Thus, in the case of weak hybridization, the second peak is somewhat similar to the spectrum of the virtual bound state formed by a localized state, with a discrete level embedded in the continuum of a conduction-electron state interacting with the localized state through hybridization. Experimentally, this is distinct in the spectra of Ce compounds with low Ce concentrations.[12] Gunnarsson and Schönhammer[26] also calculated XPS core-level spectra which are characterized by satellites reflecting the states of $4f$ electrons in the valence shells. The important parameters such as the fraction of the $4f$ occupancy, the magnitude of the hybridization, the value of U, and the renormalized energy of $4f$ states are obtained by data analyses, and they are reasonably compared with those from thermodynamic data.[10]

In the two-configuration model, it is not quite clear to how much of an extent the model reproduces the observed two-peak profiles in the valence-band spectra. This is a result of employing a smooth featureless density-of-states (DOS) curve for conduction electrons in the theoretical calculation. Takeshige, Sakai, and Kasuya,[28] Watanabe and Sakuma,[29] and Sakuma, Kuramoto, and Watanabe[30] showed that the profile of a $4f$ spectrum, particularly the second peak, is quite dependent on the magnitude and the profile of the hybridization function, $V(\varepsilon)$, which is closely related to the DOS. One possible way to apply theories to the real systems is to use $V(\varepsilon)$ calculated by means of an energy-band approximation.[27,28] The calculations using this revised model cause the Kondo peak to be smeared and the observed two-peak profile in some representative materials to be better reproduced. The calculation clearly illustrated how the two-peak profile depends on the Kondo temperature, on the value of U, and on the magnitude of hybridization.

In experiments, the constant-initial-state (CIS) spectrum of each peak in the two-peak profile near the $4d$-$4f$ resonance slightly different from one another.[4] This is the result of the Coulomb interaction between a $4f$ electron and a core hole existing in the intermediate state which implicitly modifies the energy distribution of sublevels and leads to the modification of final states which are somewhat different from those in off-resonance emission. Theoretically, Sakuma *et al.*[31] obtained different CIS curves in the limit of an infinite $4f$-$4f$ Coulomb energy, U, whereas Gunnarsson and Li[32] calculated CIS curves in the case of a finite value of U.

For finite temperatures, the occupation of sublevels of the $4f$ state is determined by the statistical distribution rule. This is important in treating the effect of the spin-orbit splitting of the $4f$ levels.[29,30] Watanabe and Sakuma[29] and Sakuma, Kuramoto, and Watanabe[30] carried out the finite-temperature calculations of the Green's function using the perturbation expansion and the noncrossing approximation.[33] Since only a single temperature corresponding to 0.03 eV is adopted, the temperature dependence of the spectral profile over a wide range of temperature is not recognizable in an explicit way. The temperature dependence of the valence-band spectra has also been calculated by Patthey *et al.*[34] The importance of removing phonon broadening in obtaining accurate $4f$ spectra has been shown experimentally by Wescke *et al.*[16] and Patthey and co-workers.[19,20,34] However, no systematic investigation of the temperature dependence appears to have been reported on the heavy fermion system.

The spin-orbit interaction of a $4f$ electron gives rise to additional features in the two-peak profile, particularly in the Kondo peak region. Experimentally, fine structures ascribable to the spin-orbit interaction were observed.[16,17,19,20,34] Theoretically, the shapes of the spectral features brought about by the spin-orbit interaction are sensitively affected by the magnitude and the energy dependence of the hybridization.[28,30,32] Since the number of $4f$ electrons in a cerium ion in the final state is practically one or zero, and the weight of the $4f^2\underline{L}^3$ configuration is small, the multiplet effect does not come into the argument of the $4f$ partial EDC. In the resonant photoemission, the multiplet splitting in the intermediate state shows up in excitation spectra. An interesting aspect of the spin-orbit interaction is the occurrence of a satellite.[29] Recently, the importance of the screening by the $5d$ electron has been emphasized by Takeshige, Sakai, and Kasuya.[35] The screening effect has been considered mostly in the form of the hybridization between the $4f$ states and other valence states. In many cases, the f-d mixing model has been used for the analyses of the two $4f$ peak profiles in the valence-band photoemission spectra and also the satellites observed in the core-level photoemission spectra. By the calculation on CeSb based on the cluster model, they explained the origin of the satellites, which appear at the higher binding-energy side of the core-level and $4f$ spectra, and are attributed to the plasmon side band corresponding to the p-d antibonding states.

The present status of theoretical studies based on the impurity Anderson Hamiltonian may be representatively summarized as above. So far, only the origin of the two-peak profile has been accepted, and others appear to be more or less still controversial. In order to present more refined data durable enough for a detailed comparison between experimental results and theoretical calculation, a kind of breakthrough in the experiments should be made. Some recent experimental investigations are aiming at this direction.[15-17,34] From the experimental point of view, it is very important to improve the sample condition. Clean surfaces are prepared, usually by a vacuum deposition, an ion bombardment, scraping with files, fracturing, and cleaving. Among these, cleaving has advantages over other sample preparations by its simplicity and its repeatability, although only a limited number of materials can be cleaved.

In this paper, we present the angle-resolved and resonant photoemission spectra of CeNi single crystals for excitation energies around the Ni $3p$ and Ce $4d$ thresholds. We selected CeNi as one of the typical cleavable mixed-valent materials. The cleaved (010) surfaces were used in experiments. From the physical point of view, CeNi is a quite interesting system, since two different types of localized electrons exist in this material. One is the $4f$ electron of Ce and the other is the $3d$ electrons of Ni. In metallic Ni, $3d$ electrons are basically itinerant and their localized nature cannot be ignored completely. The resulting effect of electron correlation produces specific aspects in photoelectron spectra such as the narrow $3d$ band and the two-hole bound-state satellite.[37-39] It is also interesting to examine many-electron effects of $3d$ electrons interacting with localized $4f$ electrons of Ce.

The intermetallic compound CeNi is a well-known mixed-valent material.[40] CeNi has the CrB-type crystal structure with lattice parameters $a = 3.77$ Å, $b = 10.46$ Å, and $c = 4.37$ Å.[41] The magnetic susceptibility is anisotropic, reflecting the CrB-type orthorhombic crystal structure. It follows the Curie-Weiss law above 200 K and makes a broad maximum around 140 K. Since the b axis is more than twice as large as other two main axes, the crystal is cleavable along the (010) plane perpendicular to the b axis. This is consistent with the fact that the bonding strength along the b axis is weaker and the energy-band dispersion is smaller than those along the a and c axes. The Kondo temperature of CeNi is about 150 K.[42] The coefficient of the electronic specific heat is measured to be 85 mJ/mole K^2, and magnetoresistance and cyclotron mass are found to be about ten times larger than those of LaNi.[43,44] Concerning with optical studies, XPS and bremsstrahlung isochromat spectroscopy (BIS) spectra have been reported by Fuggle *et al.*[10] and Hillebrecht and co-workers.[45,46] From the analyses of satellites occurring in the XPS spectra of Ce $3d$ electrons, they concluded that the electronic configuration in the ground state is formed by $4f^0L$, $4f^1\underline{L}$, and $4f^2\underline{L}^2$. The weight of the $4f^2\underline{L}^2$ configuration is small. In BIS spectra, they observed a pronounced peak just above the Fermi edge and a broadband at about 5 eV above the edge with a half-width of about 4 eV. They ascribed the peak near the Fermi edge to the state arising from the $4f^1L$ configuration and the broadband to the unresolved multiplet lines arising from the $4f^2\underline{L}$ configuration.

Recently, Yamagami and Hasegawa[47] calculated the energy-band structures of CeNi and LaNi using the self-consistent relativistic augmented-plane-wave (APW) method with exchange and correlation potentials obtained by the local-density approximation. They calculated the shapes of the Fermi surfaces and showed that their results explain the origin of the frequency branches of the de Haas–van Alphen effect of CeNi observed experimentally.[44] On the basis of this result, they suggested that $4f$ electrons are itinerant in the ground state in CeNi. The width of the Ce $4f$ band is calculated to be about 0.8 eV and the center of the $4f$ band is located 0.4 eV above the Fermi level in the ground state.

II. EXPERIMENT

Valence-band photoelectron spectra were measured with a commercially available photoelectron spectrometer, VG ADES 500, which was installed in the beam line BL-18A of the Photon Factory ring. Synchrotron radiation from the Photon Factory ring was monochromatized with a constant-deviation-angle monochromator and focused to a size of 0.8 mm in a diameter on a sample surface to excite photoelectrons. The monochromator has two different deviation angles and four spherical gratings to cover a wide photon-energy range from 8 to 150 eV. A resolving power of the monochromator is larger than 1000 when entrance and exit slits of 100 μm are used. The maximum output photon intensity around 60 eV is about 10^{11} photons/s with an energy resolution of 60 meV.

VG ADES 500 has two hemispherical photoelectron-energy analyzers; one is used for angle-resolved photoelectron spectroscopy (ARPES) and the other is used for angle-integrated photoelectron spectroscopy (AIPES). The analyzer for ARPES measurements has a resolving power of about 100 and an angular resolution of ±0.5°. In order to obtain such an energy resolution, we had to replace the entrance and exit slits of the electron-energy analyzer supplied by the manufacturer with ones with smaller diameters. We also modified several parts in the electron-counting system and in the electric circuits. The analyzer for AIPES measurements, called CLAM, has an electrostatic lens system. The resolving power of this analyzer is about 50. The lens receives photoelectrons emitted in a cone with a vertical angle of 24°. In the present experimental arrangement, where the sample surface is placed normal to the lens axis, the fraction of $k_{\parallel}$ components included in the measured total momenta of photoelectrons is less than 20% of that of $k_{\perp}$ components. Consequently, AIPES spectra in the normal-emission mode obtained in the present experiments are somewhat closely related to ARPES spectra. In spite of this, we call the spectra measured with the CLAM analyzer AIPES spectra here. The CLAM analyzer was also used for XPS by using Al $K\alpha$ and Mg $K\alpha$ radiation from an x-ray tube attached to the spectrometer. The XPS spectra are used for inspecting surface degradation. The ARPES measurements were carried out for examining the overall aspects of spectral profiles. The AIPES experiments were carried out for observing resonant photoemission. The overall instrumental resolution was determined by the width of 10–90% photoelectron intensities at the Fermi edge of Pd at room temperature. The resolution of ARPES spectra was 0.14 eV at 20-eV excitation. This instrumental energy width can be reduced to less than 0.05 eV at 15-eV excitation at liquid-nitrogen temperature. The typical energy resolution of AIPES spectra in the present study was 0.24 eV at an excitation energy of 60 and 0.36 eV at 120 eV.

The CeNi samples used in the experiments were prepared by melting component metals in an argon atmosphere to produce polycrystalline compounds. The purity of the component metals, Ce and Ni, were $3N$ and $4N$, respectively. The single-crystal CeNi was grown in a vacuum utilizing a tungsten crucible by the Czochralski pulling method. The pulling speed was 10 mm/h and the speed of rotation was 5 rpm. Part of the single crystal was pulverized and the crystal structure was confirmed to be the orthorhombic CrB-type structure by an x-ray powder diffraction pattern, from which the lattice parameters a, b, and c were obtained. The directions of the crystallographic axes were determined by the x-ray back-reflection Laue method and samples were shaped into rectangular prisms along the principal axes by a spark erosion. The clean (010) surface was obtained by cleaving the sample in a vacuum with a knife edge. Well-defined low-energy electron-diffraction (LEED) patterns were found confirming the good long-range order on the cleaved (010) surfaces. Surface contamination was examined by measuring the intensities of O 1s and C 1s core levels in XPS spectra. Since the contamination became noticeable in a few hours after cleaving, we repeated cleaving to obtain the fresh (010) surfaces. In all spectra shown here, the coverage of oxygen was less than $\frac{1}{10}$ monolayer and carbon was less than the detection limit. The LaNi samples used in the present experiments were prepared in the same procedure as CeNi samples.

In valence-band spectra for excitation energies below about 60 eV, the binding energies of observed features varied slightly upon cleaving, and intensities changed more obviously. These changes were not recognized in photoelectron spectra for higher excitation energies. We attributed these variations to small differences of surface orientations among differently cleaved surfaces. Photoemission spectra presented here were obtained using single cleaved surfaces unless otherwise noticed.

The pressure around samples during experiments was less than 5×10^{-11} Torr. All photoelectron spectra presented below, except ARPES spectra, were normalized to the intensity of incident photons. All photoemission measurements were carried out at room temperature and the location of the Fermi edge was checked repeatedly with gold films deposited on the sample holder by *in situ* evaporation.

III. RESULTS AND DISCUSSION

A. Overall aspect

Figure 1 shows the ARPES spectra of a CeNi single crystal. Photoelectrons emitted normally from the cleaved (010) surface were collected. The instrumental energy resolution was 0.14 eV at an excitation energy of 19.8 and 0.24 eV at 60.1 eV. Valence-band spectra consist of four features, which are labeled a through d in the spectrum for the 37.0-eV excitation, as an example. The photoelectron intensities at different excitation energies are normalized by the peak intensity of feature b. The binding energy of feature a remains almost constant at 0.1 eV. This feature is not like a well-defined single peak but appears to have a composite structure. The binding energies of features b, c, and d slightly change as the photon energy increases from 19.8 to 60.1 eV. However, the magnitudes of the changes are small. The intensity of feature b located at 1.0 eV in spectra for excitations below 22.8 eV becomes recognizable at excitations above 19.8 eV. This feature forms a well-defined peak and is shifted to 1.1 eV in the spectra for excitations at 49.3 and 37.0 eV. Feature c does not form a well-defined peak and has a composite structure. The binding energy of this feature shows a small amount of excitation energy dependence between 19.8 and 60.1 eV. Feature d is not clearly observed in the spectra at low excitation energy, 22.8 and 19.8 eV. Therefore, the electronic state responsible for feature d gives quite a small ionization cross section at a low excitation energy.

Since photoelectrons were emitted normally from the

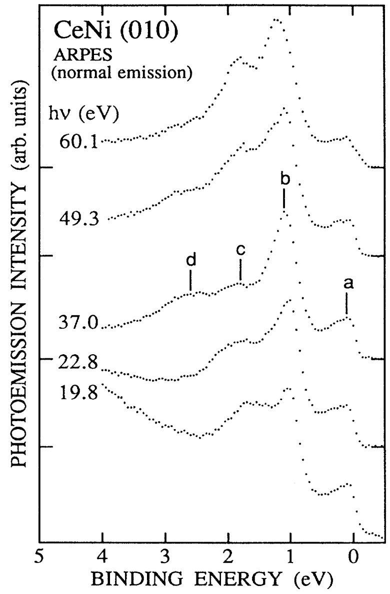

FIG. 1. Angle-resolved normal-emission photoelectron spectra of a CeNi single crystal in the valence-band region. The angle of incidence of the synchrotron radiation $\theta i = 45$ and the polarization of the electric vector is parallel to the sample surface. Features are designated as a through d. Excitation energies are indicated on the left-hand sides of the spectra.

(010) surface, the EDC's represent the energy levels lying in the Δ axis in the Brillouin zone, if the energy states we are concerned with are describable by the energy-band picture. Yamagami and Hasegawa[47] illustrated the energy-band dispersion along the Δ, Σ, *C*, *H*, *E*, *A*, Λ, and *D* axes. The energy-band structure of CeNi is similar to that of LaNi, particularly in the binding-energy region below the Fermi level. One exception is that a few extra bands are produced, owing to the existence of a 4*f* electron in CeNi. In Fig. 2, the calculated energy bands and the one-dimensional DOS along the Δ axis are reproduced. Along the Δ axis, a band without dispersion is located about 0.2 eV below the Fermi level. This band arises from the states with a strong *f*-*d* hybridization and is expected to give corresponding spectral feature in ARPES spectra at binding energy of 0.2 eV. However, we could not clearly resolve the fine structure in feature *a*, which is attributed to the spin-orbit interaction, due to a rather large instrumental energy width in the present study.

According to the energy bands shown in Fig. 2, a gap with a width of 1.2 eV exists between a sharp band near the Fermi edge and the bands originating from the 3*d* states of Ni. The bands which originate from the 3*d* states of Ni along the Δ axis are divided into two groups. One is centered around the binding energy of 1.7 eV and has an overall width of 0.3 eV. This group of bands is referred to as the upper bands. The component bands show very small amounts of dispersion, less than 0.15 eV at most in the Brillouin zone. The second group of the bands originating from the 3*d* electrons of Ni, the lower bands, exist in the binding-energy region from 2.2 to 3.7 eV. The maximum amount of dispersion expected in a component band is 0.3 eV.

The calculated partial DOS curves do not contradict the observed ARPES spectra qualitatively except for the squeeze of the Ni 3*d* bands in observed spectra, although the ionization cross section and the polarization selection rule modify the DOS curves to yield an optical DOS curve to be compared with experimental results. However, crucial discrepancies are found in the location of the features and the absence of the band gaps among the features. In the ARPES spectra shown in Fig. 1, we could not relate every feature in the spectra with the expected spectral feature from the band calculation. One possible interpretation of this discrepancy is that, since the width of the Brillouin zone along the *b* direction is about 0.60 Å^{-1}, only a small change of the excitation energy corresponds to a large transition in the momentum space and, consequently, this makes it difficult to observe the dispersion of the energy bands in ARPES spectra. Furthermore, in ARPES spectra at a higher excitation energy region, momentum and/or lifetime broadening effects may increase and each spectral feature represents the composition of many energy bands along the Δ direction within the energy resolution of the photoemission spectra.

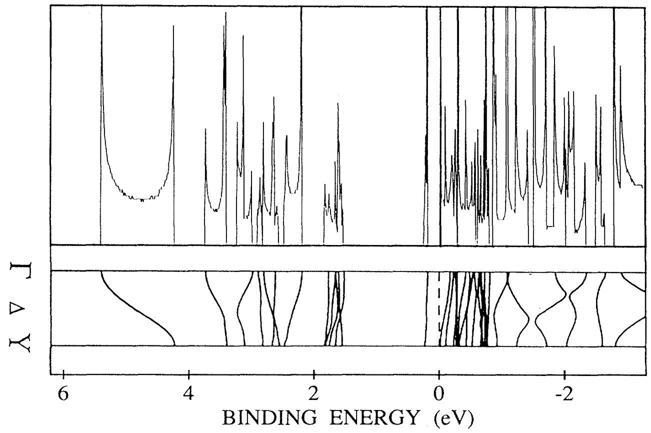

FIG. 2. Calculated energy-band dispersion and the one-dimensional density of states along the Γ-Δ-*Y* direction in CeNi.

The observed Ce 4*f*-derived feature *a* is located at 0.1 eV from the Fermi edge and has a composite structure. Qualitatively, feature *b* in Fig. 1 is a possible candidate for an emission band arising from the upper bands. Feature *c* appears to have an unresolved composite structure and could be a possible candidate for the lines arising from the lower bands if the absence of the gap between features *b* and *c* is disregarded. However, the binding energies of the features *b* and *c* are smaller than those predicted from the calculated energy bands. For feature *d*, there is no correspondence between the observed ARPES spectra and the calculated energy bands. In the calculated energy bands along the Δ axis, the band arising from 4*s* electrons of Ni and 6*s* electrons of Ce extends from 4.3 to 5.4 eV. The emission line arising from these bands is not resolved in the spectra shown in Fig. 1. The ionization cross sections of 4*s* electrons of Ni are an order of magnitude smaller than those of 3*d* electrons of Ni and 4*f* electrons of Ce for excitation energies around 20 eV.[48] The difference of the ionization cross sections increases further as the excitation energy increases. The calculated energy-band structure does not appear to explain feature *d*. This feature is not found in spectra for excitations below 25 eV. This is consistent with the result of the calculation of Yeh and Lindau[48] that the ionization cross section of a Ce 4*f* electron falls exponentially below 30 eV. As a consequence, we ascribe feature *d* to the 4*f* states of Ce.

It should be remarked that the energy-band picture could not explain the occurrence of satellites of core-levels photoemission spectra[10,45,46] and the two-peak profile of the 4*f* spectra. The two-peak profile in BIS spectra[46] also could not be explained by the energy-band picture. The 4*f* states of Ce in CeNi are better understood by a localized-electron picture and those of other electrons by a squeezed-energy-band picture.

B. 3*p*-3*d* resonance

The valence-band photoelectron spectra of a CeNi single crystal measured in the AIPES mode at excitation energies near the Ni 3*p* threshold are shown in Fig. 3. In each spectrum in Fig. 3, the locations of features are indicated by vertical bars and labeled *a* through *g* in the spectrum at an excitation energy of, for example, 60.1 eV.

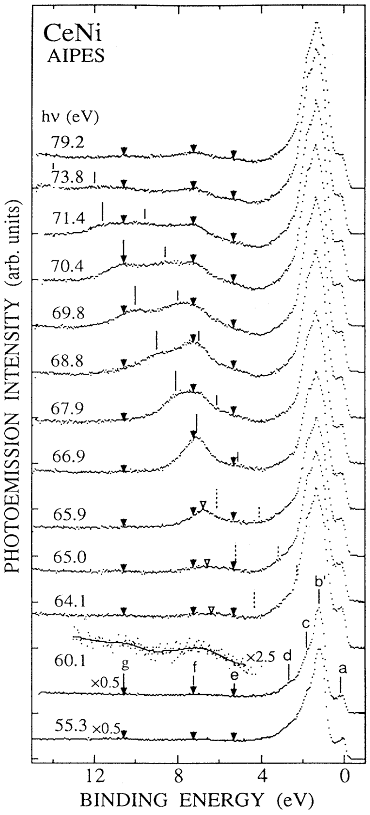

FIG. 3. Valence-band photoelectron spectra of CeNi measured in the AIPES mode by excitations near the Ni 3*p* threshold. Features are designated by letters *a* through *g*. The locations of features *e*, *f*, and *g* are indicated by black triangles. White triangles illustrate trion peaks. The locations of $M_{2,3}VV$ sCK lines observable at excitation energies above 66.9 eV are indicated by full vertical bars, and their locations expected to occur for excitations below 65.9 eV are indicated by broken vertical bars.

EDC's for 60.1- and 55.3-eV excitations in Fig. 3 are illustrated after multiplying by a factor of 0.5. The binding energies of features *a* and *b* are equal to those obtained in ARPES spectra. The binding energy of the feature labeled as *b'* in Fig. 3 does not coincide with those of feature *b* in the ARPES spectra in Fig. 1. However, feature *b'* is ascribed here to the states leading to the upper band of the Ni 3*d* states. The contribution from the states other than those on the Δ axis in the Brillouin zone may cause small changes of the binding energies of the spectral features in the AIPES mode. Features denoted as *e*, *f*, and *g* are discernible on the high binding-energy side of the main valence band. In the region between 4 and 13 eV, a part of the spectrum for 60.1-eV excitation is shown by multiplying by a factor of 2.5, where a solid curve is presented so that the existence of features *e*, *f*, and *g* is readily visible. The locations of features *e*, *f*, and *g* are indicated by black triangles in spectra for excitations at energies other than 60.1 eV. The binding energy of each feature is listed in Table I, together with the parameters *q*, Γ, and $h\nu_0$ describing the Fano line shapes for the excitation spectra of the 3*p*-3*d* resonance in Ni ions and the 4*d*-4*f* resonance in Ce ions.

The $M_{2,3}VV$ super-Coster-Kronig (sCK) lines are discernible in observed EDC's at excitation energies larger than 65.9 eV. The locations of the major features of the sCK spectra, specified by constant kinetic energies, are illustrated by full vertical bars in Fig. 3. At an excitation energy of 66.9 eV, the sCK lines completely overlap features *e* and *f*. At excitation energies lower than 65.9 eV, the sCK lines disappear. The locations expected for low excitation energies are indicated by broken vertical bars. Instead, a feature occurs below feature *f*. The location of this feature is indicated by a white triangle in each spectrum. The binding energy of this new feature is shifted toward low binding energy as the excitation energy is decreased. At the excitation energy of 65.9 eV, feature *f* merges into this new feature and only one peak is manifest at a binding energy indicated by a black triangle in the figure. For excitation energies of 65.0 and 64.1 eV, a composite profile is recognized in the region of feature *f* and the new feature. At excitation energies lower than 60.1 eV, the new feature is not resolved.

The binding energies of features *e*, *f*, and *g* are constant irrespective of the excitation energy. We assign features *e* and *f* to the two-hole bound state at a Ni ion site. The spectral profile of *e* and *f* have been interpreted as a composite structure arising from multiplet lines of the $3d^8$ configuration,[49] although the two-hole state is induced by a complete solid-state process in which two

TABLE I. Binding energies of features in EDC's of CeNi in the valence-band region. The experimentally determined values of the parameters *q* and Γ, and of the resonance energy $h\nu_0$, describing the Fano line shapes in excitation spectra for the Ni 3*p*-3*d* resonance and the Ce 4*d*-4*f* resonance are also given.

			Ni (3*p*-3*d*)			Ce (4*d*-4*f*)	
	ε_B (eV)	$h\nu$ (eV)	*q*	Γ (eV)	$h\nu$ (eV)	*q*	Γ (eV)
a	0.2				119.9	2.35	6.47
b'	1.3	68.3	0.517	6.72	120.0	2.26	4.92
c	1.8	68.5	0.531	6.41	120.1	2.25	5.41
d	2.7				120.5	2.28	5.90
e	5.3						
f	6.7	67.2	3.25	5.90			
g	10.6						

holes occur at a single ion site, owing to the multiple scattering between two $3d$ holes through the intra-atomic Coulomb interaction. Possible multiplets are ^1G, ^3F, ^1D, ^3P, and ^1S. If further interactions such as the spin-orbit effect in the core state are not negligible, more features are introduced and the two-hole bound-state spectrum has a complicated profile. In this case, two features e and f in Fig. 3, are ascribable mostly to the ^3F and ^1G, multiples, respectively.

Features e, f, and g are resonantly enhanced above the $3p$ threshold of Ni located around 65 eV in CeNi. This is clearly seen in Fig. 3. The $3p$-$3d$ resonance of the two-hole bound state and the main valence band has so far been reported for Ni and its compounds, and their resonant behavior has been investigated extensively.[50–52,56–62] However, a group of features denoted with white triangles in Fig. 3 has not been reported. We tentatively propose a model of the sCK final state with a post-collision interaction of the trion type,[54,55] where the screening of $3d$ holes is incomplete and a quasibound state consisting of two $3d$ holes and a trapped electron is formed. This will be discussed with more detailed experimental data elsewhere.[55]

The $3p$-$3d$ resonance in Ni compounds occurs at photon energies at which $3p$ core electrons are excited to the $3d$ states. There, the sCK decay of a $3p$ hole combined with $3d$ electrons takes place simultaneously as the $3p$ hole is created by photoabsorption. Since the direct emission of $3d$ electrons and their resonant emission occur at the same photon energies, both excitations interfere with each other, and the excitation spectrum has a specific shape called the Fano profile.[63] Although the Fano profile has a few different analytical forms depending on the electronic states describing systems,[35,64–67] the simplest form reproduces observed spectra in many cases. The Fano profile of the ionization cross section in its simplest form is written as

$$\sigma(h\nu,\varepsilon_B)=\sigma_0(h\nu,\varepsilon_B)\times\frac{[h\nu-h\nu_0(\varepsilon_B)+q(h\nu,\varepsilon_B)\Gamma(h\nu,\varepsilon_B)]^2}{[h\nu-h\nu_0(\varepsilon_B)]^2+[\Gamma(h\nu,\varepsilon_B)]^2} \quad (1)$$

where $h\nu$ is the photon energy and $h\nu_0$ represents the resonance energy. The cross section of the direct ionization of a valence-state electron contributing the resonance, $\sigma_0(h\nu,\varepsilon_B)$, is a smooth function of $h\nu$. It is characteristic of a feature with a binding energy ε_B in an EDC. The parameters ν_0, Γ, and q are renormalized quantities and their leading terms are approximated as follows:

$$\nu_0=\nu_c+\frac{1}{h}P\int\frac{[V_{\mathrm{sCK}}(h\nu,\varepsilon_B)]^2}{(\nu_c-\nu)}d\nu\ , \quad (2)$$

$$\Gamma=\pi[V_{\mathrm{sCK}}(\varepsilon,\varepsilon_B)]^2\ , \quad (3)$$

$$q=\frac{\langle v|\tau|c\rangle}{\pi V_{\mathrm{sCK}}\langle\varepsilon l|\tau|v\rangle}\ . \quad (4)$$

Here, $|v\rangle$, $|c\rangle$, and $|\varepsilon l\rangle$ are state vectors of a valence-shell electron, a core electron, and a photoelectron, respectively, and τ is the optical transition operator. $V_{\mathrm{sCK}}(\varepsilon,\varepsilon_B)$ represents the matrix element of the sCK transition and is roughly equal to $\langle\varepsilon l,v|1/r_{12}|v,c\rangle$. In the case of the resonant photoemission, the sum of ε_B and the energy of an emitted electron, ε, is equal to the excitation energy of $h\nu$; $h\nu_c$ is the energy of a discrete excitation of a core electron to a valence-shell state. In the present case, $|v\rangle$ and $|c\rangle$ are $|3d\rangle$ and $|3p\rangle$, respectively. Practically, the excitation-energy dependence of parameters Γ and q is ignored and they are treated as constants characteristic of features in an EDC. The excitation spectrum of a feature with a fixed binding energy in an EDC, a constant-initial-state (CIS) spectrum, consists of the resonant part given by Eq. (1), and nonresonant background arising from the overlapping tail of the cross section of the direct ionization of a valence-state electron which does not resonate.

Figure 4 shows the photon-energy dependence of photoelectron intensities for various features in the valence-band region. They are actually CIS spectra. Curves denoted a, b', c, f, and g represent CIS spectra for respective features in EDC's in Fig. 3. The photoelectron intensity at each feature was measured after subtracting a smooth background due to inelastically scattered electrons. No other data processing was made in the procedure. The excitation-energy dependence of the total photoelectron intensity obtained by integrating the intensity over the whole valence-band region is also known as *total yield* in Fig. 4. CIS spectra for features d and e are not presented. The intensity of feature d changes very little as the photon energy changes. The situation is almost the same as in the CIS spectrum for feature a in Fig. 4. Feature e is resonantly enhanced, as is obvious in Fig. 3. However, its weak intensity is crucially dependent on the procedure of the background subtraction and cannot be

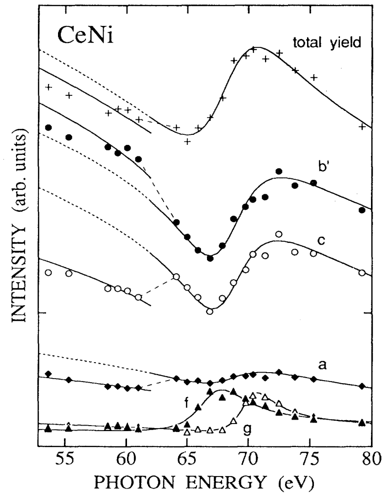

FIG. 4. Photon-energy dependence of photoelectron intensities at various features, CIS spectra, in the valence-band region near the Ni $3p$ threshold. Broken lines connect the CIS spectra for the same features in EDC's obtained using different samples. Curves denoted as a, b', c, f, and g represent CIS spectra for respective features in EDC's. Full and chain lines illustrate the Fano profiles. The curve denoted as total illustrates the yield spectrum.

performed without introducing serious errors. CIS spectra for excitation energies higher than 64 eV were obtained using a different sample from that used in measuring CIS curves for excitation energies lower than 61 eV. CIS spectra in the two different spectral regions are connected with broken lines.

The CIS spectrum of the satellite feature f shows definite resonant enhancement near the Ni $3p$ threshold. This is a common aspect of the two-hole bound state created on a Ni ion. CIS spectrum g shows a considerable enhancement. However, most of the enhancement is spurious and caused by the $M_{2,3}VV$ sCK lines superimposed on feature g. The resonance of feature g will be discussed elsewhere.[55] CIS spectra b' and c illustrate that conspicuous changes occur near the $3p$ threshold. They show dip features frequently referred to as antiresonance profiles. The existence of the dips is also noted in a difference spectrum shown in Fig. 5.

To summarize the shape of the excitation spectrum of each feature shown in Fig. 4, we assumed the Fano line shape for each excitation spectrum and evaluated the Fano parameters. They are tabulated in Table I. The Fano profiles with parameters $h\nu_0$, q, and Γ given in Table I are illustrated with full and dashed lines for spectra a, b', c, and f in Fig. 4. Since CIS spectra in the region below 61 eV cannot be connected smoothly with those above 64 eV, the curves showing the Fano profiles below 64 eV are illustrated with dashed lines. They are shifted parallel along the ordinate to yield full lines below 64 eV. Since features b' and c overlap one another appreciably, the Fano profiles exhibited in Fig. 4 may not be accurate for b' and c features. In principle, matrix elements occurring in Eqs. (2)–(4) are not equal between states responsible for two distinct features in an EDC. Thus the distinct Fano profiles result from distinct features. We ignored this in the curve fitting shown in Fig. 4, since it is impossible to isolate features b' and c from one another. We rather expect that the matrix elements describing the Fano profiles are not much different and the neglect of the overlap of features b' and c does not introduce a serious error.

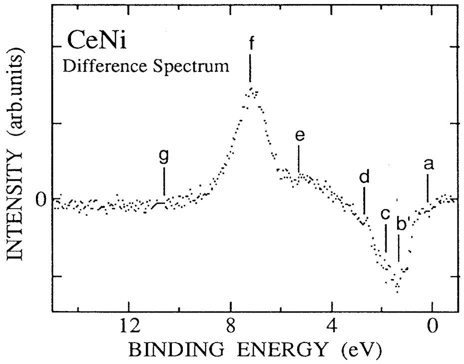

FIG. 5. Difference spectrum between on- and off-resonance EDC's near the Ni $3p$ threshold. After subtracting a smooth background due to inelastically scattered electrons, the difference spectrum is obtained by subtracting the spectrum at an excitation energy of 64.1 eV from that at an excitation energy of 66.9 eV. Vertical bars labeled a through g indicate the locations of respective features in EDC's.

The q values for features b' and c are smaller than that for feature f. On the other hand, the Γ values for features b' and c are larger than that for feature f. On the basis of the simplest interpretation of the parameters given in Eqs. (2) and (3), the straightforward consequence of these results is that V_{sCK} is larger for transitions including the states for the main $3d$ band than that for the satellite transition. The resonance energy $h\nu_0$ is slightly different between b' and c. The q value and the resonance energy of the satellite are consistent with those obtained in a Ni single crystal.[51,68] The occurrence of the valence-band satellite and the similarity of the $3p$-$3d$ resonance aspect to a Ni single crystal imply that the average number of the $3d$ holes per atom in the ground state and the degree of localization of the $3d$ states in CeNi are almost the same as in metallic Ni, in which the average $3d$ configuration is $3d^9$. However, the discussion throughout this section has been made implicitly under the assumption of the $3d^{10}$ configuration with a mixture of the $3d^9$ configuration in the ground state.[52]

Figure 5 shows a difference spectrum obtained by subtracting the off-resonance EDC at an excitation energy of 64.1 eV from the on-resonance EDC at an excitation energy of 66.9 eV. Both EDC's were measured in the AIPES mode. Vertical bars labeled a through g in the figure correspond to the respective features labeled by the same letters in Fig. 3. It is evident in the figure that the difference is negative in the main band region and positive in the satellite region. This shows the antiresonant nature of the main $3d$ band and the resonant nature of the satellite. This aspect is also found in metallic Ni (Refs. 50–54) and some Ni compounds.[56-58] The analysis of this phenomenon in CeNi will be presented elsewhere.[55]

C. $4f$ states

One of the major purposes of the present study is to draw out the $4f$ partial DOS curve. We utilized the $4d$-$4f$ resonant photoemission to obtain the partial EDC for the $4f$ state of Ce. Figure 6 shows EDC's in the valence-band region near the Ce $4d$ threshold measured in the AIPES mode. The instrumental resolution was 0.37 eV at 109.4 eV and 0.43 eV at 133.9 eV. The spectral profile at the lowest excitation energy 109.4 eV is almost the same as that at the highest excitation energy 79.2 eV in Fig. 3. Prominent features discernible in the valence-band region are indicated and labeled by letters a through f in the figure. These features are the same as those in Fig. 3. All spectral features in the main-band region are resonantly enhanced near the Ce $4d$ threshold. Satellite feature f is not enhanced by excitations just above the Ce $4d$ threshold. Among features in the main band, features a and d show salient enhancement above the threshold.

Figure 7 shows the excitation spectra for features a, b', c, d, and f. Each curve is designated as a through f which correspond to respective features in EDC's. The curve denoted as *total yield* represents the photon-energy

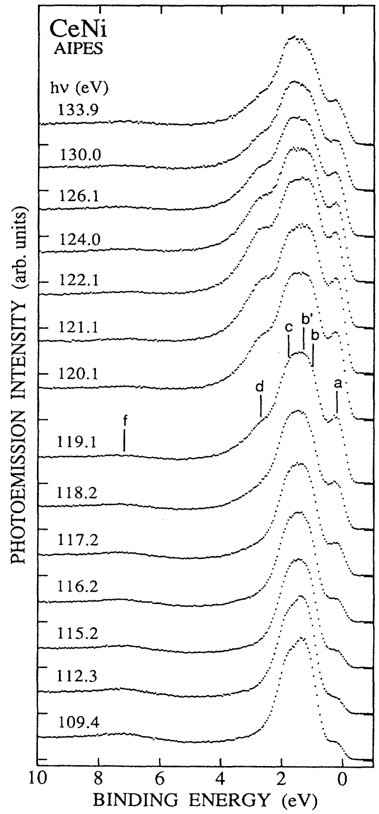

FIG. 6. Valence-band photoelectron spectra of a CeNi measured in the AIPES mode by excitations near the Ce 4*d* threshold. Features are designated as *a* through *d* and *f*. The excitation energy is indicated on the left-hand side of each spectrum.

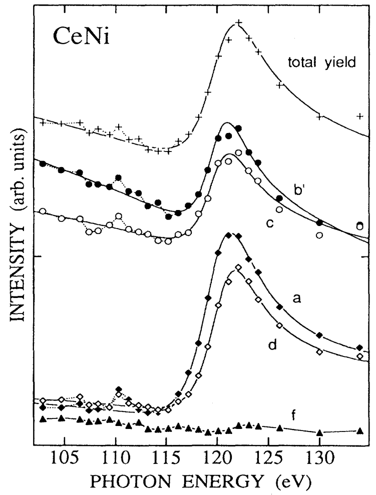

FIG. 7. Photon-energy dependence of photoelectron intensities at various features, CIS spectra, in the valence-band region near the Ce 4*d* threshold. Curves denoted as *a* through *d* and *f* represent CIS spectra for representative features in EDC's. Full lines illustrate the Fano profiles, except for curve *f*. In the region of spin-forbidden transitions, measured points are connected with dotted lines.

dependence of the total photoelectron intensity obtained by integrating the intensity of emitted electrons over the valence-band region. The excitation spectra are CIS spectra, and particularly, those for features *b'* and *c* may be affected by superposition to a considerable extent, as in the 3*p*-3*d* resonance. As we did in the case of the 3*p*-3*d* resonance, we ignore the effect of this overlap. CIS curves *a* through *d* are approximated by the Fano line shapes. The obtained *q* values, Γ values, and resonance energies are presented in Table I. The fitted Fano line shapes are illustrated with full lines running through measured points. In Ce compounds, the 4*d*-4*f* transition causes weak absorption lines due to multiplet states of the $4d^9 4f^2$ configuration in the final state, which are attainable only by spin-forbidden transitions. In the resonant photoemission, such multiplet states occur in the intermediate state. The energy distribution of the spin-forbidden multiplets in the intermediate state shows up in the excitation spectra. In Fig. 7, the presence of the multiplet lines are not resolved, but their presence is well recognized at the lower excitation-energy region. In the figure, they are illustrated by connecting measured points with dotted lines. The spin-allowed multiplets merge into the giant excitation band.

The *q* values of features *a*, *b'*, *c*, and *d* have almost the same value. The resonance energies for the different features are almost the same around 120 eV. It is quite interesting to note that the excitation spectra of the 4*d*-4*f* resonance have profiles distinct from those of the 3*p*-3*d* resonance in the main-band region. For example, curves *a* and *d* in Fig. 7 have shapes of the resonance type, whereas curves *b'* and *c* in Fig. 4 have shapes of the antiresonance type. This is well expressed as a difference in the value of *q*. The *q* value for the 4*d*-4*f* resonance is about 2.3 (the average of the values for curves *a* and *d* in Table I) and that for the 3*p*-3*d* resonance is about 0.52 (the average of the values for curves *b'* and *c*). On the other hand, the value of Γ, which is a measure of the sCK matrix element as shown by Eq. (3), is almost equal, as exhibited in Table I. Therefore, the difference in the line shapes of the excitation spectra is attributed to a difference in the ratio of the transition matrix element appearing in Eq. (4). In a more quantitative comparison, the ratio of the *q* value of the 4*d*-4*f* resonance to that of the 3*p*-3*d* resonance is estimated to be 4.4. From Eqs. (3) and (4), this ratio is approximated as

$$\frac{q(4d-4f)}{q(3p-3d)}=\left[\frac{\sigma(4d)\sigma(3d)\Gamma(3p-3d)}{\sigma(4f)\sigma(3p)\Gamma(4d-4f)}\right]^{1/2}, \tag{5}$$

where $\sigma(nl)$ is the excitation cross section of an nl electron at the resonance energy. Using the values of Γ given in Table I and $\sigma(nl)$ estimated from the calculated values,[29] we evaluated the ratio of the *q* values given in Eq. (5). The result gives a value of 4.2, which is in excellent agreement with the experimental value 4.4, given above. We find such good agreement in spite of the fact that the rigorous Fano parameters contain corrections arising from many-electron effects such as hybridization, multiplet interactions, and hopping of 3*d* electrons as well as other conduction electrons. Good agreement obtained here reveals that the Fano parameters are mostly determined by one-particle atomic orbitals, although some amounts of accidental coincidence are not ruled out.

In order to find which part of the spectrum is enhanced, we compare the standard spectrum for an excitation at 64.1 eV with an on-resonance spectrum for an excitation at 121.1 eV, and the spectrum of LaNi measured by an excitation at 64.1 eV (Fig. 8). All the spectra in the figure were measured in the AIPES mode and the spectral intensities are normalized at the highest peak. Features are indicated in the same manner as in Fig. 6. Arrows show the part where the resonant enhancement is discernible. Comparing the spectra for CeNi and LaNi at 64.1 eV, it is evident that features *a* and *d* in CeNi are caused by the emission of 4*f* electrons. The comparison of the 64.1-eV spectrum with the on-resonance spectrum show that the apparent enhancement is observed at features *a* and *d* and an additional enhancement around feature *b*. As already discussed, features *b* and *c* are ascribed to the states originating from the 3*d* states of Ni. This is consistent with the observed profile of the valence-band emission of LaNi.

In order to derive the energy distribution of the 4*f* partial density of states, it is more straightforward to obtain a difference spectrum between on- and off-resonance spectra. Figure 9 shows the difference spectra obtained by subtracting the off-resonance spectrum at 115.2-eV excitation from the spectra at excitation energies above the 4*d* electron threshold, which are indicated on the respective spectrum. The locations of the features in original EDC's are indicated on the difference spectrum for an excitation of 120.1 eV. It is obvious in the figure that the resonantly enhanced region spreads over whole valence-band region. Satellite *f* does not show resonance. It is also evident that two prominent features grow around features *a* and *d*. This shows that the 4*f* partial EDC has a two-peak profile as an overall aspect.

In order to observe the 4*f* spectrum of CeNi more precisely, the AIPES spectra on- and off-resonance were measured with an increased resolution, and the difference spectrum was obtained. The energy resolution in the difference spectrum was 0.30 eV. The result is shown in Fig. 10, which illustrates a spectrum obtained by subtracting the EDC measured at an excitation energy of 115.2 eV (antiresonance minimum) from the EDC measured at an excitation energy of 122.1 eV (resonance maximum). The standard spectrum measured by an excitation at 64.1 eV is also shown in Fig. 10. Features are indicated by letters *a* through *d*. Since the ionization cross section of a 3*d* electron of Ni decreases as the excitation energy increases, the obtained difference spectrum is affected by this excitation-energy dependence in such a way that spurious features due to the 3*d* states of Ni may emerge in the spectrum. It is quite difficult to find a right way to correct this effect. One possible way is to correct by the photon-energy dependence of Ni 3*d* partial photoionization cross section. This sort of correction was made using the calculated 3*d* partial cross sections of the Ni atom.[4] The difference spectrum obtained by using the corrected EDC's is shown by a full line in Fig. 10. This spectrum may not be the true 4*f* spectrum, since the correction may have altered the intensity of the true 4*f* partial EDC's. However, one aspect is common in the spectra with and without the correction. The additional two features indicated by arrows are manifest at binding energies of 0.85 and 1.7 eV. We conclude that the features indicated by arrows in Fig. 10 are real and not artificial ones introduced by the subtraction. In particular, the occurrence of the feature at 0.85 eV shown in Fig. 10 is also evident in the on-resonance spectrum shown in Fig. 9. The feature located at 0.85 eV in the difference spectrum is not from feature *b* found in the ARPES spec-

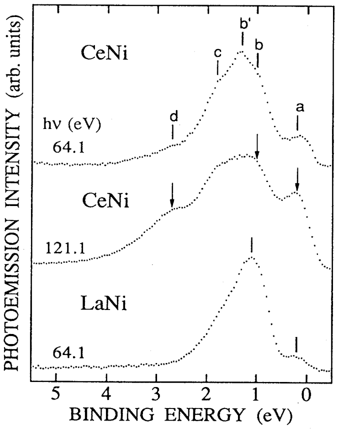

FIG. 8. Comparison between on- and off-resonance EDC's of CeNi, and with an EDC of LaNi. The excitation energy for the on-resonance spectrum is 121.1 eV and that for other two spectra 64.1 eV. Features are indicated by vertical bars with letters *a* through *d*. Arrows indicate the parts where enhancement occur.

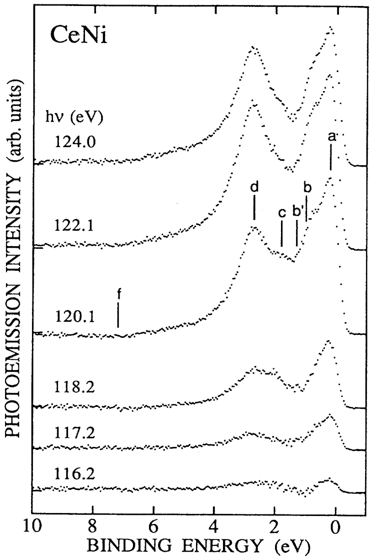

FIG. 9. Difference spectra subtracting the spectrum for an excitation at 115.2 eV, where the 4*f* photoelectron intensity is the minimum from those for excitations at various energies shown at each spectrum. The locations of features in original EDC's are indicated by vertical bars with letters *a* through *f*. Note composite structures in the two-peak features.

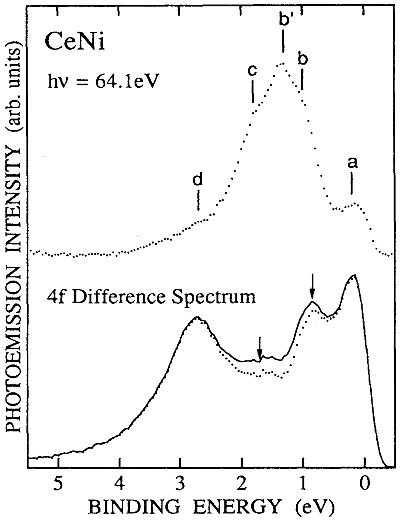

FIG. 10. Difference spectrum between the on-resonance EDC (122.1 eV) and the off-resonance EDC (115.2 eV) measured with an increased resolution. The EDC for the 64.1-eV excitation is also shown for comparison. Features in the EDC are indicated by vertical bars with letters *a* through *d*. The curve illustrated with a full line represents the difference spectrum obtained by using EDC's after the difference in the photoionization cross sections between 115.2 and 122.1 eV was corrected. Arrows indicate the locations of additional features at 0.85 and 1.7 eV in the difference spectrum.

tra shown in Figs. 1 and 8, since feature *b* is located below the Fermi edge by 1 eV. In a few photoemission experiments on Ce compounds,[4,10,66] it was found that the resonance enhancement of the 4*f* emission does not form a spectrum with an isolated two-peak structure, but with two peaks with some weak features between them. However, not much attention has been paid so far concerning the origin of this structure.

What we find concerning the 4*f* spectrum in the present study is twofold. First, the gross aspect of the spectrum is specified by the two-peak profile, one peak at the Fermi edge and the other at 2.7 eV. Second, additional features are manifest at 0.85 and 1.7 eV. In Sec. I, we have described a brief summary of representative theories based on the Anderson Hamiltonian about the occurrence of the two-peak profile. Here we interpret our 4*f* spectrum basically as described by the impurity Anderson model. According to this model, a sharp line with a spin-orbit satellite is expected to occur at the Fermi edge in the ground state. This pair of lines is often attributed to the spin-orbit-split pair of $j=\frac{5}{2}$ and $\frac{7}{2}$, occurring near the Fermi edge. Theoretically, the feature at the Fermi edge remains even at high temperatures.[30,31,34] The magnitude of the separation between the main spike and the satellite line is too small to resolve in the present study. Instead, a single broader peak that is somewhat smeared is expected to be found. We assign the feature revealed at the Fermi edge to the broadened spike feature in the present study of CeNi. As a natural consequence of the assignment mentioned above, we assign the second broad peak at 2.7 eV to the renormalized 4*f* level hybridized with the states originating from the 3*d* electrons of Ni. Since the states arising from the 3*d* electrons of Ni form comparatively narrow bands, the second peak due to the renormalized 4*f* states gives rise to a well-defined peak near the bottom of the 4*f* energy distribution. The hybridization between Ce 4*f* and Ni 4*s*, Ce 5*d* and 6*s* states will not alter the spectral feature of the 2.7-eV peak, since the DOS for those Ni 4*s*, Ce 5*d* and 6*s* states are rather flat and spread over the whole valence band, as can be seen in Fig. 2 and in comparison with the off-resonance EDC's for CeNi and LaNi in Fig. 8.

We believe that the features at 0.85 and 1.7 eV are not spurious like those introduced by the contamination of sample surfaces. As mentioned in Sec. II, we repeated cleaving to prepare fresh surfaces and confirmed this. Another possibility for the extrinsic origin is the surface effect. It was pointed out by Laubschat *et al.*[15] and Weschke *et al.*[16] that Ce atoms at surface layers give extra 4*f* emission bands to the 4*f* spectrum. They found this surface effect by comparing the 4*f* spectra obtained by the 4*d*-4*f* resonance with those by the 3*d*-4*f* resonance. However, features introduced by surface atoms are not so sharp as the ones observed in the present study. The sample surface prepared by evaporation or scraping with a diamond file consist of many facets whose direction is oriented randomly. This may cause us to observe averaged surface electronic states, i.e., the broadening of the features in EDC introduced by surface atoms.

Most of theoretical studies have dealt with the 4*f* partial DOS in the ground state or the final state of photoemission. However, the intermediate state also gives an influence on the 4*f* spectra obtained by resonant photoemission. This is because a core hole produced by photoabsorption in the intermediate state affects the final-state energy. Gunnarsson and Li[31] showed how this effect modifies the EDC to be observed experimentally. Thus it is almost impossible to draw out the real partial DOS curve for 4*f* electrons in the ground state accurately by means of optical spectra. In spite of this fact, we postulate that the 4*f* partial EDC's obtained here are very close to the 4*f* partial DOS curve. Therefore, we conclude that the additional features occurring at 0.85 and 1.7 eV are intrinsic to the bulk 4*f* spectrum.

Recently, Hüfner[21] pointed out the importance of the alternative theoretical explanation, the multichannel screening mechanism,[22,23] to interpret the two-peak profile in the valence-band spectra. The main advantage of this theory over the theories based on the impurity Anderson Hamiltonian is that it is not based on the model with adjustable parameters. The peak feature at the Fermi edge is considered to be the Ce 4*f* photoexcited final state screened by *f* electrons, and the peak at the lower binding energy is the one screened by *d* electrons. The theory assumes that the 4*f* electrons behave as band electrons and the photoexcited final state can be described by a band calculation with an appropriate approximation. If the photoemission spectra can be reproduced by a band calculation, it may not be undesirable that the observed 4*f* final state screened by *d* electrons has small features at 0.85 and 1.7 eV. However, it is not clear yet that the theory could explain the spectral features we observed in this study.

At present, the novel aspect of the $4f$ spectrum observed here cannot be analyzed further. A detailed theoretical investigation is necessary to give a definite conclusion to the origin of the additional structures between two $4f$-originated peaks.

ACKNOWLEDGMENTS

The authors are indebted to Professor Y. Murata and Dr. M. Kubota of the Institute for Solid State Physics, University of Tokyo, and the staff members of the Photon Factory, the National Laboratory for High Energy Physics, for the support and assistance for the present study. The authors thank Professor T. Kasuya for useful comments. One of the authors (T.I.) thanks Professor A. Kotani, Professor G. Kaindl, and Professor O. Sakai for stimulating discussions. The present study was partly supported by Grant-In-Aids from the Ministry of Education, Science, and Culture (Nos. 01634009, 02216108, and 63634008).

---

[1] *Handbook on Physics and Chemistry of Rare Earths,* edited by K. A. Gschneider, Jr., L. Eyring, and S. Hüfner (North-Holland, Amsterdam, 1987), Vol. 10.

[2] *Valence Instabilities,* edited by P. Wachter and H. Boppart (North-Holland, Amsterdam, 1982).

[3] *Valence Fluctuations in Solids,* edited by L. M. Falicov, W. Hanke, and M. P. Maple (North-Holland, Amsterdam, 1981).

[4] J. W. Allen, S.-J. Oh, O. Gunnarsson, K. Schönhammer, M. B. Maple, M.S. Torikachvili, and I. Lindau, Adv. Phys. **35**, 275 (1986).

[5] W. Lenth, F. Lutz, J. Barth, G. Kalkoffen, and C. Kunz, Phys. Rev. Lett. **41**, 1185 (1978).

[6] L. I. Jonansson, J. W. Allen, T. Gustafsson, I. Lindau, and S. B. M. Hagström, Solid State Commun. **28**, 53 (1978).

[7] A. Franciosi, J. H. Weaver, N. Mårtensson, and M. Croft, Phys. Rev. B **24**, 3651 (1981).

[8] H. Sugawara, A. Kakizaki, I. Nagakura, T. Ishii, T. Komatsubara, and T. Kasuya, J. Phys. Soc. Jpn. **51**, 915 (1982).

[9] D. J. Peterman, J. H. Weaver, and M. Croft, Phys. Rev. B **25**, 5530 (1982).

[10] J. C. Fuggle, F. U. Hillebrecht, Z. Zolnierek, R. Lässer, C. Freiburg, O. Gunnarsson, and K. Schönhammer, Phys. Rev. B **27**, 7330 (1983).

[11] R. D. Parks, S. Raaen, M. L. den Boer, Y.-S. Chang, and G. P. Williams, J. Magn. Magn. Mater. **47&48**, 163 (1985).

[12] K. Naito, Y. Onuki, T. Komatsubara, T. Miyahara, H. Kato, S. Sato, K. Soda, S. Asaoka, and T. Ishii, J. Phys. Soc. Jpn. **55**, 4349 (1986).

[13] K. Soda, T. Mori, Y. Onuki, T. Komatsubara, and T. Ishii, J. Phys. Soc. Jpn. **57**, 1699 (1988).

[14] A. Fujimori, T. Miyahara, T. Koide, T. Shidara, H. Kato, H. Fukutani, and S. Sato, Phys. Rev. B **38**, 7789 (1988).

[15] C. Laubschat, E. Weschke, C. Holtz, M. Domke, O. Strebel, and G. Kaindl, Phys. Rev. Lett. **65**, 1639 (1990).

[16] E. Weschke, C. Laubschat, T. Simmons, M. Domke, O. Strebel, and G. Kaindl, Phys. Rev. B **44**, 8304 (1991).

[17] J. J. Joyce, A. J. Arko, J. Lawrence, P. C. Canfield, Z. Fisk, R. J. Bartlett, and J. D. Thompson, Phys. Rev. Lett. **68**, 236 (1992).

[18] D. M. Wieliczka, C. G. Olson, and D. W. Lynch, Phys. Rev. Lett. **52**, 2180 (1984).

[19] F. Patthey, B. Delly, W.-D. Schneider, and Y. Baer, Phys. Rev. Lett. **55**, 1518 (1985).

[20] F. Patthey, W.-D. Schneider, Y. Baer, and B. Delley, Phys. Rev. B **34**, 2967 (1986).

[21] S. Hüfner, Z. Phys. B **86**, 241 (1992).

[22] M. R. Norman, D. D. Koelling, and A. J. Freeman, Phys. Rev. B **31**, 6251 (1985).

[23] P. S. Reiseborough, Solid State Commun. **57**, 721 (1986).

[24] K. Okada and A. Kotani, in *Core Level Spectroscopy in Condensed Systems,* edited by J. Kanamori and A. Kotani (Springer-Verlag, Berlin, 1987), p. 64.

[25] A. Fujimori, Phys. Rev. B **28**, 4489 (1983).

[26] O. Gunnersson and K. Schönhammer, Phys. Rev. B **28**, 4315 (1983).

[27] O. Gunnersson and K. Schönhammer, Phys. Rev. B **31**, 4815 (1985).

[28] M. Takeshige, O. Sakai, and T. Kasuya, J. Magn. Magn. Mater. **52**, 363 (1985).

[29] T. Watanabe and A. Sakuma, Phys. Rev. B **31**, 6320 (1985).

[30] A. Sakuma, Y. Kuramoto, and T. Watanabe, Phys. Rev. B **34**, 2231 (1986).

[31] A. Sakuma, Y. Kuramoto, T. Watanabe, and C. Horie, J. Magn. Magn. Mater. **52**, 393 (1985).

[32] O. Gunnarsson and T. C. Li, Phys. Rev. B **36**, 9488 (1987).

[33] Y. Kuramoto, Z. Phys. B **53**, 37 (1983).

[34] F. Patthey, J.-M. Imer, W.-D. Schneider, H. Beck, and Y. Baer, Phys. Rev. B **42**, 8864 (1990).

[35] M. Takeshige, O. Sakai, and T. Kasuya, J. Phys. Soc. Jpn. **60**, 666 (1991).

[36] N. E. Bickers, Rev. Mod. Phys. **59**, 845 (1987).

[37] L. C. Davis, J. Appl. Phys. **59**, R25 (1986), and references therein.

[38] D. R. Penn, Phys. Rev. Lett. **42**, 921 (1979).

[39] S. C. Wu, C. K. Lok, J. Sokolov, F. Jona, and A. Taleb-Ibrahmi, Phys. Rev. B **39**, 1058 (1989).

[40] D. Gignoux, F. Givord, R. Lemaire, and F. Tassett, J. Less-Common Metals **94**, 165 (1983).

[41] J. J. Finney and A. Rosenzweig, Acta Crystallogr. **14**, 69 (1961).

[42] Y. Isikawa, K. Mori, A. Fujii, and K. Sato, J. Phys. Soc. Jpn. **55**, 3165 (1986).

[43] Y. Isikawa, K. Mori, T. Mizushima, A. Fujii, H. Takeda, and K. Sato, J. Magn. Magn. Mater. **70**, 385 (1987).

[44] Y. Onuki, Y. Kurosawa, K. Maezawa, I. Uehara, Y. Isikawa, and K. Sato, J. Phys. Soc. Jpn. **58**, 3705 (1989).

[45] F. U. Hillebrecht, J. C. Fuggle, G. A. Sawatzky, M. Campagna, O. Gunnarsson, and K. Schönhammer, Phys. Rev. B **30**, 1777 (1985).

[46] F. U. Hillebrecht and M. Campagna, Ref. 1, Chap. 70.

[47] H. Yamagami and A. Hasegawa, J. Phys. Soc. Jpn. **60**, 1011 (1991).

[48] J. J. Yeh and I. Lindau, At. Data Nucl. Data Tables **32**, 1 (1985).

[49] N. Mårtensson, R. Nyholm, and B. Johansson, Phys. Rev. B **30**, 2245 (1984).

[50] C. Gillot, Y. Ballu, J. Paigné, J. Lecante, K. P. Jain, P. Thiry, R. Pinchaux, Y. Pétroff, and L. M. Falicov, Phys. Rev. Lett. **39**, 1632 (1977).

[51] J. Barth, G. Kalkoffen, and C. Kunz, Phys. Lett. **74A**, 360

(1979).

[52]W. Eberhardt and E. W. Plummer, Phys. Rev. B **21**, 3245 (1980).

[53]J. Igarashi, J. Phys. Soc. Jpn. **59**, 348 (1990).

[54]J. Igarashi, J. Phys. Soc. Jpn. **54**, 2762 (1985).

[55]A. Kakizaki, T. Kashiwakura, T. Kinoshita, T. Ishii, Y. Isikawa, S. Suzuki, T. Okane, and S. Sato (unpublished).

[56]A. Kakizaki, K. Sugeno, T. Ishii, H. Sugawara, I. Nagakura, and S. Shin, Phys. Rev. B **28**, 1026 (1983).

[57]S.-J. Oh, J. W. Allen, I. Lindau, and J. C. Mikkelssen, Jr., Phys. Rev. B **26**, 4845 (1982).

[58]A. Fujimori, F. Minami, and S. Sugano, Phys. Rev. B **29**, 5225 (1984).

[59]L. C. Davis and L. A. Feldkamp, Phys. Rev. B **23**, 6239 (1981).

[60]L. A. Feldkamp and L. C. Davis, Phys. Rev. Lett. **43**, 151 (1979).

[61]L. C. Davis, Phys. Rev. B **25**, 2912 (1982).

[62]J. C. Parlebas, A. Kotani, and J. Kanamori, Solid State Commun. **41**, 439 (1982); J. Phys. Soc. Jpn. **51**, 124 (1982).

[63]U. Fano, Phys. Rev. **124**, 1866 (1961).

[64]A. Shibatani (Kotani) and Y. Toyozawa, J. Phys. Soc. Jpn. **25**, 335 (1968).

[65]A. Kotani and Y. Toyozawa, in *Synchrotron Radiation*, edited by C. Kunz (Springer-Verlag, Heidelberg, 1979), p. 196.

[66]C.-O. Almbladh and L. Hedin, in *Handbook on Synchrotron Radiation*, edited by E. E. Koch (North-Holland, Amsterdam, 1983), Vol. 1b, p. 607.

[67]Y. Yafet, Phys. Rev. B **21**, 5023 (1980).

[68]K. Soda, T. Mori, S. Asaoka, T. Ishii, Y. Onuki, and T. Komatsubara, J. Phys. Soc. Jpn. **56**, 2486 (1987).